



# The 7-year MAXI/GSC X-Ray Source Catalog in the High Galactic Latitude Sky (3MAXI)

T. Kawamuro<sup>1,13</sup> , Y. Ueda<sup>2</sup> , M. Shidatsu<sup>3</sup>, T. Hori<sup>2</sup> , M. Morii<sup>4</sup>, S. Nakahira<sup>3</sup>, N. Isobe<sup>5</sup>, N. Kawai<sup>6</sup> , T. Mihara<sup>3</sup>, M. Matsuoka<sup>3</sup>, T. Morita<sup>2</sup>, M. Nakajima<sup>7</sup>, H. Negoro<sup>8</sup>, S. Oda<sup>2</sup>, T. Sakamoto<sup>9</sup>, M. Serino<sup>9</sup>, M. Sugizaki<sup>3</sup>, A. Tanimoto<sup>2</sup> , H. Tomida<sup>5</sup>, Y. Tsuboi<sup>10</sup> , H. Tsunemi<sup>11</sup>, S. Ueno<sup>5</sup>, K. Yamaoka<sup>12</sup>, S. Yamada<sup>2</sup>, A. Yoshida<sup>9</sup>, W. Iwakiri<sup>3</sup>, Y. Kawakubo<sup>9</sup>, Y. Sugawara<sup>5</sup> , S. Sugita<sup>6</sup>, Y. Tachibana<sup>6</sup>, and T. Yoshii<sup>6</sup>

<sup>1</sup>National Astronomical Observatory of Japan, Osawa, Mitaka, Tokyo 181-8588, Japan; [taiki.kawamuro@nao.ac.jp](mailto:taiki.kawamuro@nao.ac.jp)

<sup>2</sup>Department of Astronomy, Kyoto University, Kitashirakawa-Oiwake-cho, Sakyo-ku, Kyoto 606-8502, Japan

<sup>3</sup>MAXI team, RIKEN, 2-1, Hirosawa, Wako-shi, Saitama 351-0198, Japan

<sup>4</sup>The Institute of Statistical Mathematics, 10-3 Midori-cho, Tachikawa, Tokyo 190-8562, Japan

<sup>5</sup>Institute of Space and Astronautical Science, Japan Aerospace Exploration Agency, 3-1-1 Yoshinodai, Chuo, Sagamihara, Kanagawa 252-5210, Japan

<sup>6</sup>Department of Physics, Tokyo Institute of Technology, 2-12-1 Ookayama, Meguro-ku, Tokyo 152-8551, Japan

<sup>7</sup>School of Dentistry at Matsudo, Nihon University, 2-870-1, Sakaecho-nishi, Matsudo, 271-8587, Chiba, Japan

<sup>8</sup>Department of Physics, Nihon University, 1-8 Kanda-Surugadai, Chiyoda-ku, Tokyo 101-8308, Japan

<sup>9</sup>College of Science and Engineering, Department of Physics and Mathematics, Aoyama Gakuin University,

5-10-1 Fuchinobe, Chuo-ku, Sagamihara, Kanagawa 252-5258, Japan

<sup>10</sup>Department of Physics, Faculty of Science & Engineering, Chuo University, 1-13-27 Kasuga, Bunkyo, Tokyo 112-8551, Japan

<sup>11</sup>Department of Earth and Space Science, Graduate School of Science, Osaka University, 1-1 Machikaneyama-cho, Toyonaka, Osaka 560-0043, Japan

<sup>12</sup>Institute for Space-Earth Environmental Research (ISEE), Nagoya University, Furo-cho, Chikusa-ku, Nagoya, Aichi 464-8601, Japan

Received 2018 April 22; revised 2018 June 22; accepted 2018 June 29; published 2018 October 15

## Abstract

We present the third MAXI/GSC catalog in the high Galactic latitude sky ( $|b| > 10^\circ$ ) based on the 7-year data from 2009 August 13 to 2016 July 31, complementary to that in the low Galactic latitude sky ( $|b| < 10^\circ$ ) (Hori et al. 2018). We compile 682 sources detected at significances of  $s_{D,4-10\text{ keV}} \geq 6.5$  in the 4–10 keV band. A two-dimensional image fit based on the Poisson likelihood algorithm ( $C$ -statistics) is adopted for the detections and constraints on their fluxes and positions. The 4–10 keV sensitivity reaches  $\approx 0.48$  mCrab, or  $\approx 5.9 \times 10^{-12}$  erg  $\text{cm}^{-2} \text{s}^{-1}$ , over half of the survey area. Compared with the 37-month Hiroi et al. (2013) catalog, which adopted a threshold of  $s_{D,4-10\text{ keV}} \geq 7$ , the source number increases by a factor of  $\sim 1.4$ . The fluxes in the 3–4 keV and 10–20 keV bands are further estimated, and hardness ratios (HRs) are calculated using the 3–4 keV, 4–10 keV, 3–10 keV, and 10–20 keV band fluxes. We also make the 4–10 keV light curves in 1-year bins for all the sources and characterize their variabilities with an index based on a likelihood function and the excess variance. Possible counterparts are found from five major X-ray survey catalogs by *Swift*, *Uhuru*, *RXTE*, *XMM-Newton*, and *ROSAT*, as well as an X-ray galaxy cluster catalog (MCXC). Our catalog provides the fluxes, positions, detection significances, HRs, 1-year bin light curves, variability indices, and counterpart candidates.

**Key words:** catalogs – galaxies: active – galaxies: clusters: general – surveys – X-rays: galaxies

**Supporting material:** figure set, machine-readable tables, tar.gz files

## 1. Introduction

The Monitor of All-sky X-ray Image (MAXI; Matsuoka et al. 2009) on board the International Space Station (ISS) has been successfully monitoring the X-ray sky since its launch in 2009 August. The Gas Slit Camera (GSC) on the MAXI (Mihara et al. 2011), covering the 2–30 keV band, surveys the sky with two instantaneous fields of view of  $3.0^\circ \times 160^\circ$  separated by  $84^\circ$ . Rotating its fields of view with a period of 92 minutes according to the orbital motion of the ISS, the GSC eventually covers a large fraction of the sky (95%) in 1 day (Sugizaki et al. 2011).

As an all-sky X-ray survey mission, the MAXI/GSC has achieved the best sensitivity in the 4–10 keV band, which is not covered by the *ROSAT* all-sky survey ( $< 2$  keV; Truemper 1982) and hard X-ray ( $> 10$  keV) surveys performed with the *Swift*/BAT (Gehrels et al. 2004) and *INTEGRAL*/IBIS (Winkler et al. 2003). The 4–10 keV X-rays have good penetrating power up to a column density of  $\log N_{\text{H}}/\text{cm}^{-2} \sim 23$ , providing samples less

biased against the absorption than the *ROSAT* catalogs. Also, this energy band has an advantage in detecting sources with “soft” spectra above 4 keV (e.g., a steep power law), compared with hard X-rays above 10 keV. Thus, the MAXI/GSC survey is complementary to other X-ray surveys conducted in different energy bands.

A variety of X-ray sources have been detected by accumulating the MAXI/GSC data on different timescales. The MAXI Alert system automatically informs us of variabilities within a few days (Negoro et al. 2012, 2016). As a result, a number of new X-ray transients have been discovered (e.g., Morii et al. 2013; Serino et al. 2015; Shidatsu et al. 2017a), and recurrent activities of known sources have been captured (e.g., Isobe et al. 2015). Most of them are Galactic objects. Also, systematic surveys focusing on a few-month variability provided unique samples including objects undetected in shorter- or longer-timescale surveys (e.g., tidal disruption events; Kawamuro et al. 2016a). To extract the best sensitivities for most sources, high and low Galactic latitude sky catalogs were produced by integrating all the MAXI/GSC data available then (7 months to 7 years; Hiroi et al. 2011, 2013; Hori et al. 2018).

<sup>13</sup> JSPS fellow (PD).

Particularly, the high-latitude catalogs have been used as a basis to study extragalactic objects, mainly active galactic nuclei (AGNs; e.g., Ueda et al. 2011, 2014; Terashima et al. 2015; Inoue & Tanaka 2016; Isobe et al. 2016; Abeysekara et al. 2017).

In this paper, we present the third MAXI/GSC X-ray source catalog in the high Galactic latitude sky ( $|b| > 10^\circ$ ) constructed from the first 7-year data. This is an extension of the 7-month and 37-month catalogs (Hiroi et al. 2011, 2013) and is complementary to the 7-year low Galactic latitude catalog (Hori et al. 2018). The catalog consists of sources detected in the 4–10 keV data, to be consistent with the previous works. We also estimate the fluxes in the 3–4 keV and 10–20 keV bands of each source and calculate the hardness ratios (HRs) among the four bands (3–4 keV, 4–10 keV, 3–10 keV, and 10–20 keV) to obtain spectral information. The 10–20 keV band flux is new information that was unavailable in the previous high Galactic latitude catalogs. Also, by analyzing time-sliced images, we make the 4–10 keV light curves in 1-year bins for all the detected sources. Transiently brightened sources undetected in the 7-year image are found in these time-sliced data, which are summarized as a transient event catalog in the Appendix.

This paper is organized as follows. Section 2 describes analysis procedures from data reduction to source detection and provides the source catalog. In Section 3 we make the 1-year bin light curves and search for transient events. Cross-matching with other X-ray catalogs is performed in Section 4.1. Then, we discuss the statistical properties of the cataloged sources in Section 5 based on the fluxes, HRs, and the time variability index. The  $\log N$ – $\log S$  relation is also shown in Section 5.3. We summarize our work in Section 6.

## 2. Catalog Construction

### 2.1. Overview of the MAXI/GSC Data

We analyze the MAXI/GSC event data from 2009 August 13 to 2016 July 31 provided by RIKEN (rev. 1.8),<sup>14</sup> focusing on those at high Galactic latitudes ( $|b| > 10^\circ$ ). The same data-screening criteria as adopted by Hori et al. (2018; see their Section 2) are applied. We exclude the data taken with four GSCs (GSC3, GSC6, GSC9, and GSCa) out of all 12 GSCs from the analysis. GSC6, GSC9, and GSCa were operated only for  $< 1$  yr, which is too short to establish a reliable background model (see below). The GSC3 data are highly contaminated by background counts owing to defects of the veto counters (Sugizaki et al. 2011), and they are also subject to large calibration uncertainties in the position determination. Apart from them, the GSC0 data since 2013 June 15 are not used because they are affected by gas leakage. We select the 4–10 keV band for source detection by considering the high quantum efficiency and low background rate (Mihara et al. 2011).

Here we summarize main differences of the third MAXI/GSC high Galactic latitude catalog compared with the second one (Hiroi et al. 2013). A major advantage is the increased photon statistics (37 months to 84 months). Others are improved calibration of the background (the non-X-ray background plus

the cosmic X-ray background) and the point-spread function (PSF), as detailed in Hori et al. (2018). These are key components in our image analysis (Section 2.2.1). It was found that the background event rates well correlate with the rates of simultaneous events in the carbon-anode cells and the tungsten-anode cells for particle veto (i.e., VC-counts; Mihara et al. 2011; Sugizaki et al. 2011). This correlation was already used to reproduce the background events in Hiroi et al. (2013). In the new background model, we also take into account the direction of movement of the ISS with respect to the Earth (to the north or south), on which the background-to-VC-count correlation is found to largely depend (see Figure 2 of Shidatsu et al. 2017b; Hori et al. 2018). In return, the 10–20 keV data can now be reliably utilized, which were not analyzed in the previous work. Also, an updated PSF database as a function of energy and detector position of each counter (see the Appendix of Hori et al. 2018) is implemented to the MAXI event simulator, “*maxisim*” (Eguchi et al. 2009).

### 2.2. Image Analysis

Here we briefly describe the image analysis for source detection, which is essentially the same as that adopted in Hiroi et al. (2013). In the event files, each photon has information of sky position (RA and decl.), which is converted from an estimated position in the detector along the anode direction and the pointed direction of the collimator at the detected time. We first divide the all-sky image into 768 tangentially projected images of  $14^\circ 0' \times 14^\circ 0'$  size (binned by  $0^\circ 1' \times 0^\circ 1'$ ), whose central coordinates are determined by the HEALPix system (Górski et al. 2005). Then, we apply the processes described in the following subsections to each projected image. This consists of two steps: (1) making a tentative source-candidate list based on simple photon statistics, and (2) determining the flux, significance, and position by image fitting with a model composed of the background and PSFs. To model the background image, we produce simulated background events that have 10 times more counts than those of real data, using the MAXI/GSC background generator (Eguchi et al. 2009).

#### 2.2.1. Source Finding

We first make a source-candidate list to be used as the input to the image-fit process. Combining the real data (consisting of source and background events) and the simulated background data, we calculate “nominal significances” as  $(\text{real} - \text{background counts}) / \sqrt{\text{real counts}}$ , where those counts are integrated within a radius of  $1^\circ$  around each image bin. From this “significance map,” we identify a bin showing the highest significance as the position of the first source candidate. After masking a  $3^\circ$  radius circular region centered on the source-candidate position, we again search for another candidate. This is iterated until no peak is found with a significance larger than  $15\sigma$ . Subsequently, to find fainter sources, we adjust the normalization of the background model so that the counts of the masked real and masked background data become identical, assuming that the contribution from remaining fainter sources to the observed counts is ignorable. Such fine-tuning of the background (typically by  $< 5\%$ ) is required owing to systematic uncertainties in the background model and fluctuation of the level of the cosmic X-ray background. Then, we repeat the same source-finding procedures above by lowering the detection threshold to  $5.0\sigma$ . Merging the source-candidate lists

<sup>14</sup> The official day of the MAXI first light is 2009 August 15 ([http://iss.jaxa.jp/en/kiboexp/ef/maxi/maxi\\_first\\_light.html](http://iss.jaxa.jp/en/kiboexp/ef/maxi/maxi_first_light.html)), when both the GSCs and Solid-state Slit Cameras (Tomida et al. 2011) started the operation. However, because the activation of all the GSCs was already completed on 2009 August 13, the GSC data taken earlier than the first-light day are available.

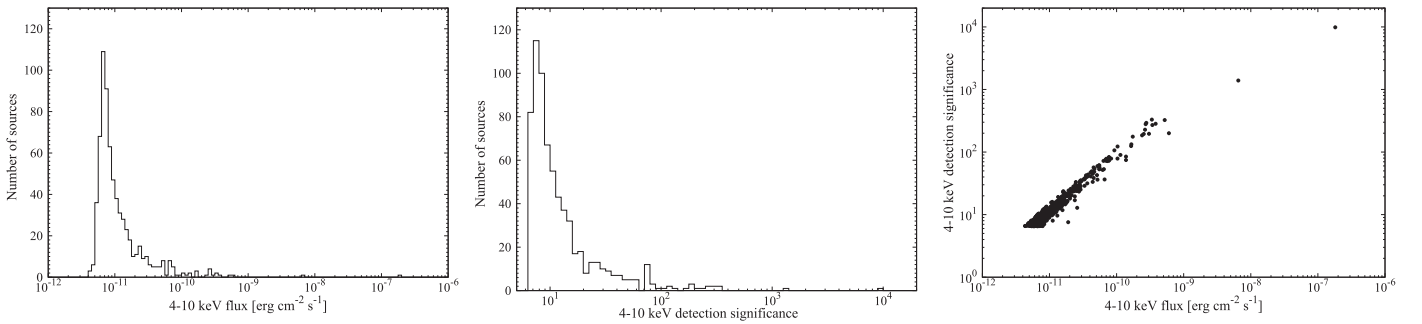


**Figure 1.** Histogram of the 4–10 keV flux (left), that of the detection significance (middle), and their correlation plot (right).

from all the images, we sometimes find multiple sources within  $1^\circ$ , which is smaller than a typical size (FWHM) of the MAXI/GSC PSF ( $\sim 1.5^\circ$ ). This happens because there are some overlap areas among the projected images. In such cases, we only leave the source candidate located closest to the center of the analyzed image.

### 2.2.2. Image Fit

The PSFs for the source candidates are constructed from simulated photon events produced by the MAXI simulator (Eguchi et al. 2009) with exactly the same observing conditions as for the real data. We assume a point source having the same spectrum as the Crab Nebula. Throughout this paper, we assume that the Crab Nebula has a power law with a photon index of 2.1 and a normalization of  $10 \text{ photons cm}^{-2} \text{ s}^{-1} \text{ keV}^{-1}$  at 1 keV, absorbed with a hydrogen column density of  $2.6 \times 10^{21} \text{ cm}^{-2}$ . The fluxes are  $3.96 \times 10^{-9} \text{ erg cm}^{-2} \text{ s}^{-1}$ ,  $1.21 \times 10^{-8} \text{ erg cm}^{-2} \text{ s}^{-1}$ ,  $8.51 \times 10^{-9} \text{ erg cm}^{-2} \text{ s}^{-1}$ , and  $1.61 \times 10^{-8} \text{ erg cm}^{-2} \text{ s}^{-1}$  in the 3–4 keV, 4–10 keV, 10–20 keV, and 3–10 keV bands, respectively, which correspond to “1 Crab.”

Then, we fit the PSF and background models to the real image. Here we restrict the fitting region to an inner  $11^\circ 0' \times 11^\circ 0'$  area, because the outer region may be affected by sources located just outside the edge of the  $14^\circ 0' \times 14^\circ 0'$  region. The fluxes and peak positions of the PSFs and the normalization of the background are left as free parameters. We determine these parameters by the Poisson maximum likelihood (ML) algorithm (C-statistics), using the MINUIT software package. The likelihood function is defined as

$$C \equiv 2 \sum_{i,j} \mathcal{L}(i, j), \quad (1)$$

where

$$\mathcal{L}(i, j) = \begin{cases} M(i, j) - D(i, j) + D(i, j) \{ \ln D(i, j) - \ln M(i, j) \} & (D_{i,j} > 0) \\ M(i, j) & (D_{i,j} = 0). \end{cases}$$

The observed data and model at the  $(i, j)$  bin are denoted with  $D(i, j)$  and  $M(i, j)$ , respectively. The  $1\sigma$  statistical error of each parameter is estimated by finding a value when the likelihood function ( $C$ ) is increased from its minimum by unity. The detection significance is defined as (best-fit flux)/(its lower-side  $1\sigma$  error). We confirm that the lower- and upper-side errors are generally consistent with each other. This is expected because the number of counts is large enough to follow a Gaussian distribution. Since we measure a relative count rate to

that that would be expected from the Crab Nebula spectrum, the flux is given in “Crab” units.

### 2.2.3. Iteration of Source Finding and Image Fit

Some sources located near bright sources could be missed in the first source-candidate list because we masked out the  $3^\circ$  circular region around each source candidate. To make our source finding complete, we repeat the source-finding process (Section 2.2.1) by using a new significance map (smoothed residual map) where the best-fit model (background plus PSFs) obtained in the above image-fit process (Section 2.2.2) is adopted as the background. Then, including those new source candidates detected with nominal significances of  $\geq 5.5\sigma$ , we perform the image fit again. This provides the final source catalog.

## 2.3. Catalog

We detect 682 sources with 4–10 keV detection significances of  $s_{D,4-10 \text{ keV}} \geq 6.5$  at high Galactic latitudes ( $|b| > 10^\circ$ ). Table 1 gives our source catalog. Considering the improved calibration of the background and PSF models (Section 2.1), and following the 7-year “low” Galactic latitude catalog (Hori et al. 2018), we have decided to lower the detection threshold from  $s_{D,4-10 \text{ keV}} \geq 7$ , which was adopted in the 37-month catalog (Hiroi et al. 2013), to  $s_{D,4-10 \text{ keV}} \geq 6.5$  in our new catalog. The number of the cataloged sources increases by a factor of  $\approx 1.4$  compared with Hiroi et al. (2013), where 500 sources were listed. If the same threshold of  $s_{D,4-10 \text{ keV}} \geq 7$  as in Hiroi et al. (2013) is adopted, the source number of our catalog becomes 615. The counterpart candidate is listed in Table 2, as detailed in Section 4.1. The sensitivity limit achieved for 50% of the survey area is  $\sim 0.48 \text{ mCrab}$ , or  $\sim 5.9 \times 10^{-12} \text{ erg cm}^{-2} \text{ s}^{-1}$  (Section 5.3). Figure 1 shows the distribution of the flux and detection significance in the 4–10 keV band, as well as their correlation. Figure 2 plots the statistical errors in the position ( $1\sigma_{\text{stat}}$ ) against the detection significance. The spatial distribution in the Galactic coordinates is shown in Figure 3. The classification of sources in this figure is detailed in Section 4.1.

### 2.3.1. Spurious Source Fraction

The detection threshold should be determined to maximize the number of detected sources while suppressing that of spurious sources caused by statistical and/or systematic fluctuations of the data to an acceptable level. We estimate the number of spurious sources in our catalog by counting that of negative signals with the same detection threshold, assuming that their significance distribution is symmetrical in positive and negative sides around the background level. We first search the significance maps produced from the data and the best-fit models for negative-signal

**Table 1**  
X-Ray Properties of Sources in the Third MAXI/GSC Catalog

No. (1)	3MAXI (2)	R.A. (3)	Decl. (4)	$\sigma_{\text{stat}}$ (5)	$S_{\text{D},4-10\text{keV}}$ (6)	$f_{4-10\text{keV}}$ (7)	$S_{\text{D},3-4\text{keV}}$ (8)	$f_{3-4\text{keV}}$ (9)	$S_{\text{D},10-20\text{keV}}$ (10)	$f_{10-20\text{keV}}$ (11)	$f_{3-10\text{keV}}$ (12)	HR1 (13)	HR2 (14)	HR3 (15)	$\text{TS}_{\text{var}}$ (16)	$\sigma_{\text{HS}}^2$ (17)
1	J0001-684	0.251	-68.463	0.215	11.1	$7.74 \pm 0.70$	9.8	$2.19 \pm 0.23$	1.2	$3.00 \pm 2.60$	$9.93 \pm 0.74$	$0.07 \pm 0.07$	$-0.29 \pm 0.40$	$-0.27 \pm 0.40$	2.29	$-0.045 \pm 0.037$
2	J0004-348	1.037	-34.897	0.161	7.8	$7.36 \pm 0.94$	11.2	$2.87 \pm 0.26$	2.0	$6.67 \pm 3.41$	$10.23 \pm 0.98$	$-0.09 \pm 0.08$	$0.13 \pm 0.26$	$0.10 \pm 0.26$	4.98	$-0.047 \pm 0.059$
3	J0006+727	1.602	72.742	0.097	12.5	$10.39 \pm 0.83$	16.1	$4.36 \pm 0.27$	1.8	$5.94 \pm 3.25$	$14.75 \pm 0.87$	$-0.12 \pm 0.05$	$-0.10 \pm 0.27$	$-0.14 \pm 0.27$	10.26	$0.043 \pm 0.054$
4	J0009+109	2.462	10.938	0.146	9.5	$8.53 \pm 0.90$	7.9	$2.10 \pm 0.27$	4.5	$15.75 \pm 3.48$	$10.63 \pm 0.94$	$0.14 \pm 0.08$	$0.45 \pm 0.10$	$0.47 \pm 0.09$	14.78	$0.067 \pm 0.069$
5	J0010+323	2.621	32.390	0.177	7.3	$7.63 \pm 1.04$	8.4	$2.58 \pm 0.31$	...	$0.39(<4.49)$	$10.21 \pm 1.09$	$-0.02 \pm 0.09$	$-0.86 \pm 1.33$	$-0.86 \pm 1.32$	5.64	$-0.071 \pm 0.080$
6	J0011-113	2.804	-11.311	0.089	12.7	$10.24 \pm 0.81$	10.7	$2.48 \pm 0.23$	...	$0.58(<3.69)$	$12.72 \pm 0.84$	$0.15 \pm 0.06$	$-0.85 \pm 0.74$	$-0.84 \pm 0.78$	8.93	$0.009 \pm 0.030$
7	J0011-292	2.962	-29.231	0.137	9.6	$8.02 \pm 0.84$	12.1	$2.93 \pm 0.24$	2.1	$6.83 \pm 3.28$	$10.95 \pm 0.87$	$-0.06 \pm 0.07$	$0.10 \pm 0.24$	$0.08 \pm 0.24$	9.36	$0.034 \pm 0.066$
8	J0012-313	3.132	-31.351	0.235	7.6	$6.46 \pm 0.85$	5.5	$1.32 \pm 0.24$	2.6	$8.49 \pm 3.29$	$7.78 \pm 0.88$	$0.23 \pm 0.11$	$0.30 \pm 0.19$	$0.35 \pm 0.18$	6.98	$-0.020 \pm 0.061$
9	J0012-154	3.139	-15.433	0.177	7.2	$5.60 \pm 0.78$	9.7	$2.16 \pm 0.22$	1.5	$4.60 \pm 3.06$	$7.76 \pm 0.81$	$-0.08 \pm 0.09$	$0.08 \pm 0.34$	$0.06 \pm 0.34$	6.81	$-0.038 \pm 0.097$
10	J0016-825	4.145	-82.587	0.171	7.2	$5.29 \pm 0.73$	3.4	$0.82 \pm 0.24$	2.2	$5.49 \pm 2.48$	$6.11 \pm 0.77$	$0.36 \pm 0.14$	$0.19 \pm 0.23$	$0.26 \pm 0.22$	5.02	$-0.072 \pm 0.087$
11	J0021+286	5.319	28.601	0.119	10.1	$9.92 \pm 0.98$	8.9	$2.58 \pm 0.29$	2.0	$7.94 \pm 3.92$	$12.50 \pm 1.02$	$0.11 \pm 0.07$	$0.07 \pm 0.25$	$0.09 \pm 0.25$	10.20	$0.076 \pm 0.075$
12	J0022-193	5.733	-19.356	0.150	10.6	$8.25 \pm 0.78$	10.5	$2.39 \pm 0.23$	3.7	$11.66 \pm 3.12$	$10.64 \pm 0.81$	$0.06 \pm 0.07$	$0.34 \pm 0.13$	$0.35 \pm 0.12$	5.37	$-0.034 \pm 0.041$
13	J0027+075	6.762	7.597	0.193	7.4	$6.51 \pm 0.88$	2.9	$0.74 \pm 0.25$	...	$1.00(<4.30)$	$7.25 \pm 0.91$	$0.48 \pm 0.14$	$-0.64 \pm 0.97$	$-0.59 \pm 1.08$	9.65	$0.024 \pm 0.098$
14	J0029+127	7.269	12.736	0.206	7.7	$7.09 \pm 0.93$	5.6	$1.50 \pm 0.27$	2.8	$10.05 \pm 3.58$	$8.59 \pm 0.97$	$0.21 \pm 0.11$	$0.34 \pm 0.17$	$0.38 \pm 0.16$	4.48	$-0.059 \pm 0.075$
15	J0035-791	8.974	-79.178	0.121	13.0	$8.83 \pm 0.68$	13.4	$3.03 \pm 0.23$	3.8	$9.19 \pm 2.38$	$11.86 \pm 0.72$	$-0.02 \pm 0.05$	$0.19 \pm 0.13$	$0.19 \pm 0.13$	24.40	$0.092 \pm 0.057$
16	J0039+231	9.850	23.117	0.170	6.6	$6.02 \pm 0.92$	4.3	$1.21 \pm 0.27$	2.4	$8.45 \pm 3.55$	$7.23 \pm 0.96$	$0.24 \pm 0.13$	$0.33 \pm 0.20$	$0.38 \pm 0.19$	3.41	$-0.090 \pm 0.089$
17	J0041-093	10.455	-9.318	0.026	54.1	$46.94 \pm 0.87$	54.2	$15.02 \pm 0.28$	7.2	$22.56 \pm 3.12$	$61.96 \pm 0.91$	$0.01 \pm 0.01$	$-0.19 \pm 0.07$	$-0.18 \pm 0.07$	7.99	$-0.000 \pm 0.002$
18	J0042+412	10.668	41.238	0.044	31.6	$36.63 \pm 1.16$	32.4	$11.97 \pm 0.37$	4.6	$19.84 \pm 4.30$	$48.60 \pm 1.22$	$0.00 \pm 0.02$	$-0.13 \pm 0.11$	$-0.13 \pm 0.11$	6.38	$-0.004 \pm 0.005$
19	J0048+319	12.051	31.900	0.057	20.4	$21.47 \pm 1.05$	7.9	$2.42 \pm 0.31$	6.0	$24.01 \pm 4.04$	$23.89 \pm 1.09$	$0.49 \pm 0.05$	$0.23 \pm 0.08$	$0.31 \pm 0.08$	15.54	$0.009 \pm 0.014$
20	J0048-732	12.057	-73.205	0.094	14.6	$17.22 \pm 1.92$	13.9	$3.71 \pm 0.27$	3.9	$11.07 \pm 2.83$	$20.93 \pm 1.94$	$0.21 \pm 0.06$	$-0.04 \pm 0.14$	$-0.00 \pm 0.14$	47.97	$0.227 \pm 0.096$

**Note.** Column (1): source number. Column (2): MAXI name determined from the source coordinates. Columns (3)–(4): R.A. and decl. in units of degrees. Column (5):  $1\sigma$  statistical error of the position in units of degrees. Note that the systematic error is not taken into consideration. Columns (6)–(7), (8)–(9), and (10)–(11): detection significance and 7-year averaged flux in units of  $10^{-12}$  erg  $\text{cm}^{-2}$   $\text{s}^{-1}$  for each energy band. When a  $1\sigma$  error is larger than the best-fit value, the  $1\sigma$  upper limit is represented. The conversion factor from Crab units into erg  $\text{cm}^{-2}$   $\text{s}^{-1}$  units in the 4–10 keV, 3–4 keV, and 10–20 keV bands is  $1.21 \times 10^{-11}$  erg  $\text{cm}^{-2}$   $\text{s}^{-1}$  mCrab $^{-1}$ ,  $3.96 \times 10^{-12}$  erg  $\text{cm}^{-2}$   $\text{s}^{-1}$  mCrab $^{-1}$ , and  $8.51 \times 10^{-12}$  erg  $\text{cm}^{-2}$   $\text{s}^{-1}$  mCrab $^{-1}$ , respectively. Column (12): the flux in the 3–10 keV band. Note that the factor of  $1.61 \times 10^{-11}$  erg  $\text{cm}^{-2}$   $\text{s}^{-1}$  mCrab $^{-1}$  is usable for the conversion. Column (13): hardness ratios calculated from the fluxes in the 3–4 keV and 4–10 keV bands. Note that they are derived from the flux in units of Crab. Columns (14)–(15): same as Column (13), but for the 4–10 keV and 10–20 keV bands and the 3–10 keV and 10–20 keV bands. Column (16): time variability index (see the text for the definition). The hypothesis that the flux does not vary can be ruled out for  $\text{TS}_{\text{var}} > 18.48$  at the 99% confidence level. Column (17): excess variance.

(This table is available in its entirety in machine-readable form.)

**Table 2**  
Possible Counterparts of the Third MAXI/GSC Sources

No. (1)	MAXI 3MAXI (2)	Counterpart					Flag (8)	Note (9)
		Name (3)	R.A. (4)	Decl. (5)	$z$ (6)	Type (7)		
1	J0001–684	...	...	...	...	...	...	...
2	J0004–348	...	...	...	...	...	...	...
3	J0006+727	...	...	...	...	...	...	...
4	J0009+109	Mrk 1501	2.629	10.975	0.0893	Blazar	BR	...
5	J0010+323	RXC J0011.7+3225	2.935	32.417	0.1073	Galaxy Cluster	MR	...
6	J0011–113	1RXS J001124.6–112843	2.853	–11.479	...	Dwarf Nova	R	...
7	J0011–292	...	...	...	...	...	...	...
8	J0012–313	...	...	...	...	...	...	...
9	J0012–154	MACS J0011.7–1523	2.928	–15.389	0.378	Galaxy Cluster	M	...
10	J0016–825	...	...	...	...	...	...	...
11	J0021+286	RXC J0020.6+2840	5.17	28.675	0.094	Galaxy Cluster	MR	...
12	J0022–193	...	...	...	...	...	...	...
13	J0027+075	...	...	...	...	...	...	...
14	J0029+127	...	...	...	...	...	...	...
15	J0035–791	2MASX J00341665–7905204	8.57	–79.089	0.074	Sy1	BR	...
16	J0039+231	...	...	...	...	...	...	...
17	J0041–093	ABELL 85	10.408	–9.342	0.0555	Galaxy Cluster	BMR	...
18	J0042+412	SWIFT J0042.7+4111	10.668	41.2	...	confused source	B	...
19	J0048+319	Mrk 348	12.196	31.957	0.015	Blazar	BX	...
20	J0048–732	...	...	...	...	...	...	...

**Note.** Column (1): source number. Column (2): MAXI name. Columns (3)–(7): available information of the counterpart (name, R.A., and decl. in units of degrees, redshift, and source type). Column (8): cross-matching flag: B, U, X, M, N, and R represents that the source has more than one counterpart in BAT105, 4U, XTEASMLONG, MCXC, XMMSL2, and 1RXS, respectively. The counterpart name listed in Column (3) is quoted from the catalog expressed by the leftmost letter in this column. Column (9): note related to the identification of the counterpart. (A) The auto-matching identifies a galaxy cluster, but this is likely inconsistent with the significant variability ( $TS_{\text{var}} = 87$ ). Then, we select a star as a plausible candidate of the counterpart. (B) We automatically find an obscured AGN from BAT105 as the counterpart, but the very soft property is not so common to such objects. Then, we find a bright object, CXO J092418.2–314217, in a *Swift*/XRT soft X-ray image. According to a study by Tomsick et al. (2017), it can be classified as an LMXB or a CV, and here we representatively adopt the LMXB. (C) One of the brightest galaxies is selected for the most plausible counterpart.

(This table is available in its entirety in machine-readable form.)

candidates. Then, we create their PSF models through simulation and perform image fitting by allowing their normalizations to be negative. We find that our catalog may contain 26 spurious sources with  $s_{D,4-10 \text{ keV}} \geq 6.5$ , which corresponds to 4% of the total 682 sources. If we adopt  $s_{D,4-10 \text{ keV}} \geq 6$  as the threshold, the number of spurious sources drastically increases to 58 sources, 8% of the total 766 sources. Thus, we select  $s_{D,4-10 \text{ keV}} = 6.5$  as the threshold. Depending on the scientific purpose, catalog users can choose a more conservative threshold; the estimated fraction of spurious sources becomes 3% (17/615) for  $s_{D,4-10 \text{ keV}} \geq 7$  and 0.6% (3/477) for  $s_{D,4-10 \text{ keV}} \geq 8$ .

### 2.3.2. Hardness Ratios

To calculate HRs of the detected sources, we determine the fluxes in the 3–4 keV and 10–20 keV bands in the following way. Tangentially projected images in these bands are produced from the event files. We prepare the input source list for the image fit from our catalog produced above. For completeness, here we also include the source candidates whose detection significances were less than  $6.5\sigma$  in the 4–10 keV band. We then perform an image fit to the image in the 3–4 keV or 10–20 keV band using this source list. During the fitting process, the positions are fixed at those determined in the 4–10 keV band. This process is repeated by adding new source candidates found in the smoothed residual map with nominal significances (see Section 2.2.1) above  $5.5\sigma$ . Eventually, we find no new sources detected with significances above  $6.5\sigma$  in the 3–4 keV or 10–20 keV band but not included in the above catalog based on the 4–10 keV band survey. The

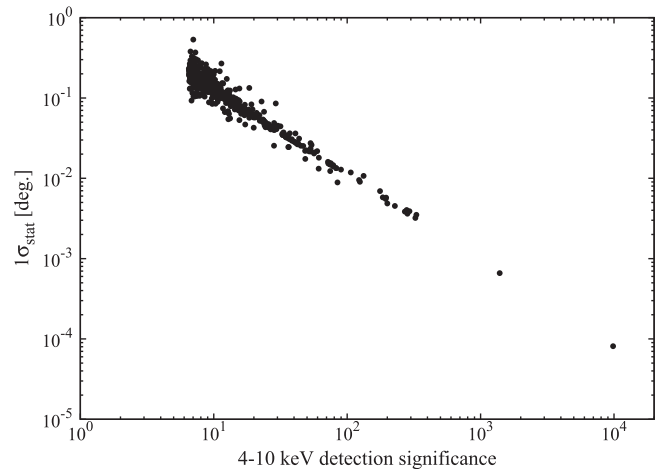


**Figure 2.** Positional error ( $1\sigma_{\text{stat}}$ ) as a function of the 4–10 keV detection significance ( $s_{D,4-10\text{keV}}$ ).

3–10 keV fluxes are also calculated from the 3–4 keV and 4–10 keV fluxes obtained above by assuming the Crab-like spectrum. We define the HR as

$$\text{HR} = \frac{f_H - f_S}{f_H + f_S}, \quad (2)$$

where  $f_H$  and  $f_S$  correspond to the hard- and soft-band fluxes, respectively, in Crab units. The catalog lists three HRs: HR1

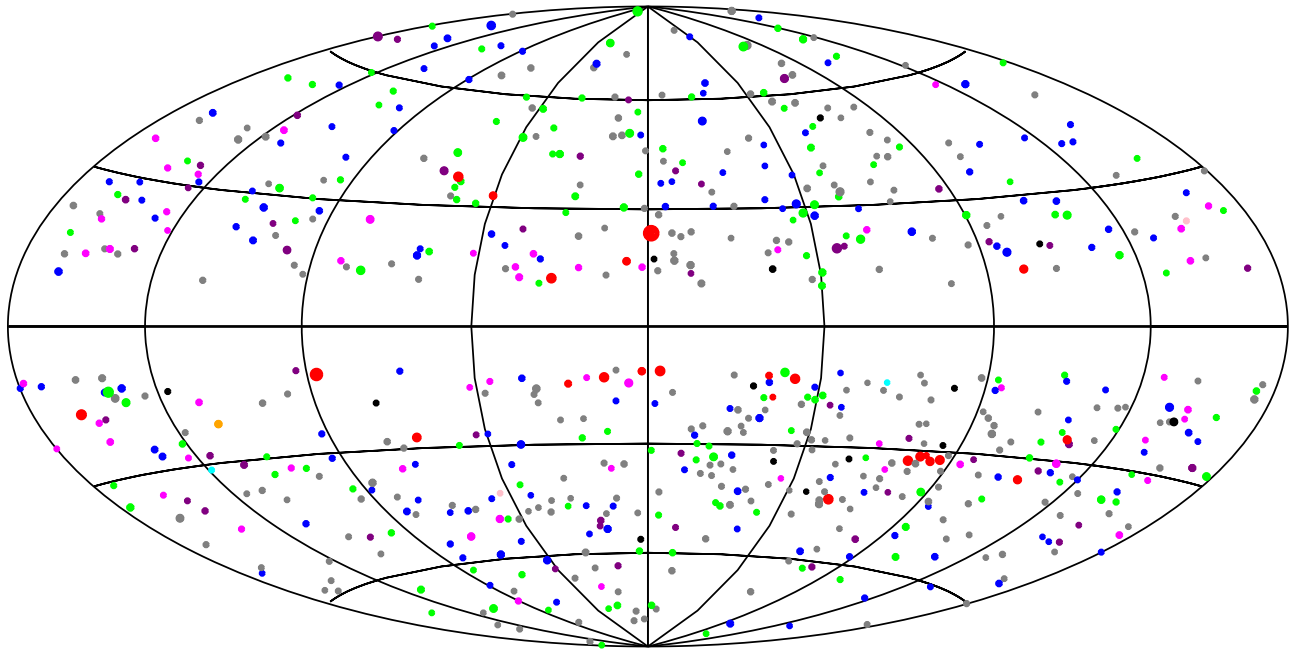


**Figure 3.** Spatial distribution of the detected 682 X-ray sources in Galactic coordinates. The center corresponds to  $(l, b) = (0^\circ, 0^\circ)$ . The radii of the circles are proportional to the logarithm of the 4–10 keV flux. According to the results of catalog cross-matching (Section 4.1), a color is assigned to each source type: unidentified X-ray sources in BAT105 (black), galaxies (cyan), galaxy clusters (green), Seyfert galaxies (blue), blazars (purple), cataclysmic variables/stars (magenta), X-ray binaries (red), pulsars (pink), confused sources (orange), and sources without any counterparts in the reference catalogs (gray).

(3–4 keV, 4–10 keV), HR2 (4–10 keV, 10–20 keV), and HR3 (3–10 keV, 10–20 keV).

To deduce the spectral shape from the HRs, we calculate the relation between the HRs and spectra parameters by assuming an absorbed power-law model. The parameters are a photon index ( $\Gamma$ ) and an intrinsic hydrogen column density ( $N_{\text{H}}$ ). We also take into account a representative Galactic absorption of  $N_{\text{H}}^{\text{Gal}} = 2.5 \times 10^{20} \text{ cm}^{-2}$  in addition to the intrinsic one. This column density roughly corresponds to the minimum value over the high Galactic latitude sky ( $|b| > 10^\circ$ ; Daltabuit & Meyer 1972) and should be considered as a lower limit for extragalactic objects. We confirmed, however, that the spatial variation in the total Galactic column ( $N_{\text{H}}^{\text{Gal}} < 2 \times 10^{21} \text{ cm}^{-2}$  for  $|b| > 10^\circ$ ) has little effect on the following results. The source redshift is not considered for simplicity. We generate, through the MAXI on-demand tool,<sup>15</sup> the 7-year averaged MAXI/GSC response file and calculate the predicted count rates in these bands for given spectral parameters. We consider two cases: a power-law model with and without an intrinsic absorption. The Galactic absorption is taken into account in both cases. In the former case, we fix  $\Gamma = 1.8$  and vary  $\log N_{\text{H}}/\text{cm}^{-2}$  in a range of 20–24, whereas in the latter case, we fix  $N_{\text{H}} = 0$  and vary  $\Gamma$  in a range of 1–3. The results are plotted in the left panels of Figure 4. We also calculate the conversion factors from the flux in Crab units to that in the CGS system ( $\text{erg cm}^{-2} \text{ s}^{-1}$ ), which are presented in the right panels of Figure 4. For an unabsorbed power law with  $\Gamma = 1.8$ , HR1 = 0.0749, HR2 = 0.115, and HR3 = 0.136, and the conversion factors are  $4.00 \times 10^{-12} \text{ erg cm}^{-2} \text{ s}^{-1} \text{ mCrab}^{-1}$ ,  $1.24 \times 10^{-11} \text{ erg cm}^{-2} \text{ s}^{-1} \text{ mCrab}^{-1}$ ,  $1.65 \times 10^{-11} \text{ erg cm}^{-2} \text{ s}^{-1} \text{ mCrab}^{-1}$ , and  $8.74 \times 10^{-12} \text{ erg cm}^{-2} \text{ s}^{-1} \text{ mCrab}^{-1}$  in the 3–4 keV, 4–10 keV, 10–20 keV, and 3–10 keV bands, respectively.

### 3. Time-sliced Image Analysis

#### 3.1. 4–10 keV Light Curves

Flux variability provides us with a key to deduce the nature of X-ray sources; for example, we can use the fact that many compact objects (e.g., X-ray binaries and AGNs) are transients, whereas extended sources like galaxy clusters are more persistent.

Here we produce the 4–10 keV light curves in 1-year binning. We split the real, background, and PSF data used in the catalog construction into each year and perform image fitting for each time-sliced data set. We adopt the same observation period as those in the catalog construction, and therefore the time bins in 2009 and 2016 have smaller sizes than the other bins. In addition to the cataloged sources, there may be transient sources that can be detected at significances above  $6.5\sigma$  in a 1-year image but not in the 7-year accumulated data. Thus, we systematically search for such sources (see Section 3.2) and incorporate their PSFs in the image fitting. The positions of the cataloged sources are fixed at those determined from the whole 7-year data, while the positions of the newly detected transients are at those determined in the time bin where their detection significances are the highest. Then, we construct the light curves of the individual sources by fitting the normalizations of their PSFs and the background model.

In addition to the statistical flux errors, we derive the systematic error, which may remain because we do not consider possible time variation of the PSF profile in our PSF database. We simply determine the systematic error so that the Crab light curve is consistent with 1 Crab over the 7 years. This is a conservative way to estimate the systematic errors, since the X-ray flux of Crab is not perfectly constant (Wilson-Hodge et al. 2011) and its variability is included in the estimation. As shown in the left panel of Figure 5, adding 1.4% error is found to be sufficient. This value is taken into account in all the light curves as the systematic errors. This systematic uncertainty is comparable to that derived

<sup>15</sup> <http://maxi.riken.jp/mxondem/>

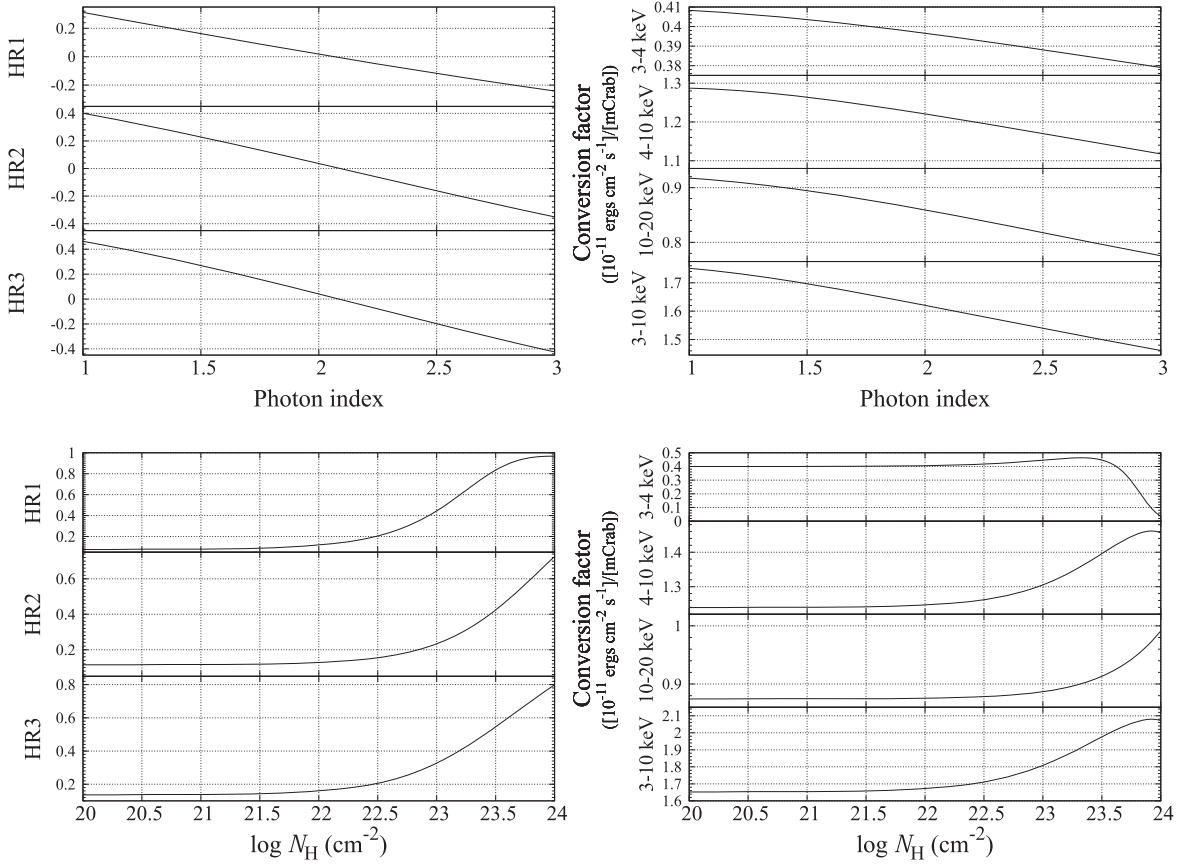


**Figure 4.** Top left: relation between photon index and HRs: HR1 (3–4 keV, 4–10 keV), HR2 (4–10 keV, 10–20 keV), and HR3 (3–10 keV, 10–20 keV). No absorption other than the Galactic one ( $N_{\text{H}}^{\text{Gal}} = 2.5 \times 10^{20} \text{ cm}^{-2}$ ) is considered. Top right: conversion factor in units of  $10^{-11} \text{ erg cm}^{-2} \text{ s}^{-1} \text{ mCrab}^{-1}$  as a function of photon index. Bottom left: relation between hydrogen column density and HRs for an absorbed power-law model with a photon index of 1.8. Bottom right: conversion factor in units of  $10^{-11} \text{ erg cm}^{-2} \text{ s}^{-1} \text{ mCrab}^{-1}$  as a function of hydrogen column density.

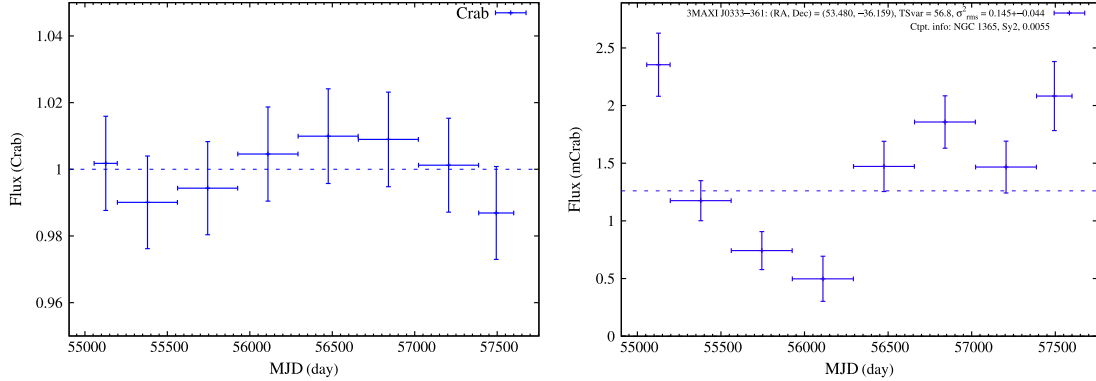


**Figure 5.** Left: 1-year-bin light curve of the Crab Nebula in the 4–10 keV band. The dashed line denotes the 7-year-averaged Crab flux, which is defined as 1 Crab. Right: same as the left panel, but for NGC 1365 (AGN) in units of mCrab. The counterpart information (name, type, and redshift) is listed in the legend. Both light curves take account of a systematic flux error of 1.4% (see the text).

in Hori et al. (2018), 1.6%, and much reduced compared with that in the 37-month data ( $\sim 10\%$ ; Hiroi et al. 2013; Kawamuro et al. 2016a). This improvement can be ascribed to the sophisticated PSF model. Among the light curves (Figure 6), we present, as an interesting case, the NGC 1365 (AGN) one in the right panel of Figure 5, which shows the strong variability by a factor of  $\sim 5$  within the 7-year. Individual light-curve plots and full light-curve data are published in an online tar.gz supplement.

We characterize the light curves in two steps. First, to statistically examine whether a light curve is constant or varies,

we adopt a likelihood-based method as used in Nolan et al. (2012). This is more appropriate than the simple least chi-squared method when the photon statistics follow the Poisson distribution, and therefore it can be used for faint sources as well as for bright ones. We calculate a test statistic defined as

$$\text{TS}_{\text{var}} = 2 \sum_i \frac{\Delta F_i^2}{\Delta F_i^2 + f^2 F_{\text{const}}^2} [\log \mathcal{L}'_i(F_i) - \log \mathcal{L}'_i(F_{\text{const}})], \quad (3)$$

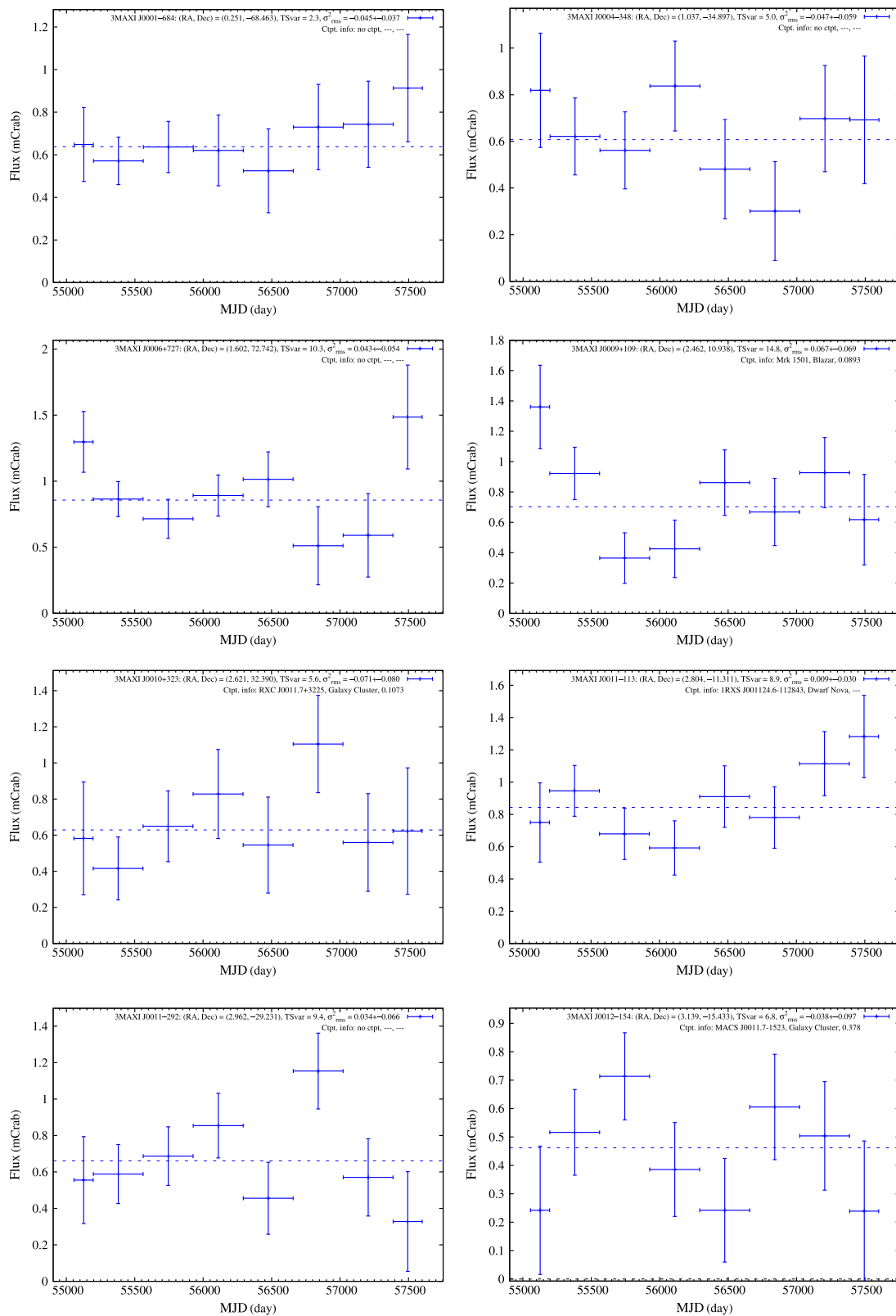


**Figure 6.** Light curves in the 4–10 keV band during the 7 years in units of mCrab. The blue dashed line denotes the 7-year averaged flux. The counterpart information (name, type, and redshift if available) is denoted in each figure. Individual plots and data for the light curves are available from the online supplementary tar.gz file. The complete figure set (86 images) is available in the online journal.

(The complete figure set (86 images) is available.)

**Table 3**  
Properties of Transient Events

No. (1)	MAXI								Counterpart				
	3MAXIt (2)	R.A. (3)	Decl. (4)	$\sigma_{\text{stat}}$ (5)	$s_{\text{D},4-10\text{keV}}$ (6)	$f_{4-10\text{keV}}$ (7)	$\text{TS}_{\text{var}}$ (8)	$\sigma_{\text{rms}}^2$ (9)	Name (10)	R.A. (11)	Decl. (12)	$z$ (13)	Type (14)
1	J0051–735	12.954	–73.562	0.080	11.7	$48.4 \pm 2.8$	1721.87	$5.395 \pm 0.782$	RX J0052.1–7319	13.058	–73.322	...	HMXB
2	J0912–649	138.047	–64.911	0.060	20.8	$72.3 \pm 3.5$	3486.07	$5.652 \pm 0.329$	MAXI J0911–655	138.010	–64.868	...	millisecond X-ray pulsar
3	J1257+014	194.471	1.489	0.118	9.4	$18.6 \pm 1.9$	367.453	$3.253 \pm 0.849$	NGC 4845	194.505	1.576	0.004110	Sy2/tidal disruption event
4	J1357–095	209.257	–9.509	0.139	13.6	$25.5 \pm 1.8$	758.631	$5.708 \pm 0.835$	Swift J1357.2–0933	209.320	–9.544	...	LMXB

**Note.** Column (1): source number. Column (2): MAXI transient source name. Columns (3)–(4): R.A. and decl. in units of degrees. Column (5):  $1\sigma$  statistical error of the position in units of degrees. Note that the systematic error is not taken into consideration. Columns (6)–(7): detection significance and flux in units of  $10^{-12}$  erg  $\text{cm}^{-2}$   $\text{s}^{-1}$ . Column (8): time variability index (see the text for the definition). Column (9): excess variance. Columns (10)–(14): available information of the counterpart (name, R.A. and decl. in units of degrees, redshift, and source type), which is based on the *Swift*/BAT Hard X-ray Transient Monitor catalog (<https://swift.gsfc.nasa.gov/results/transients/>). The data file of the light curves is available from the online supplementary tar.gz file.

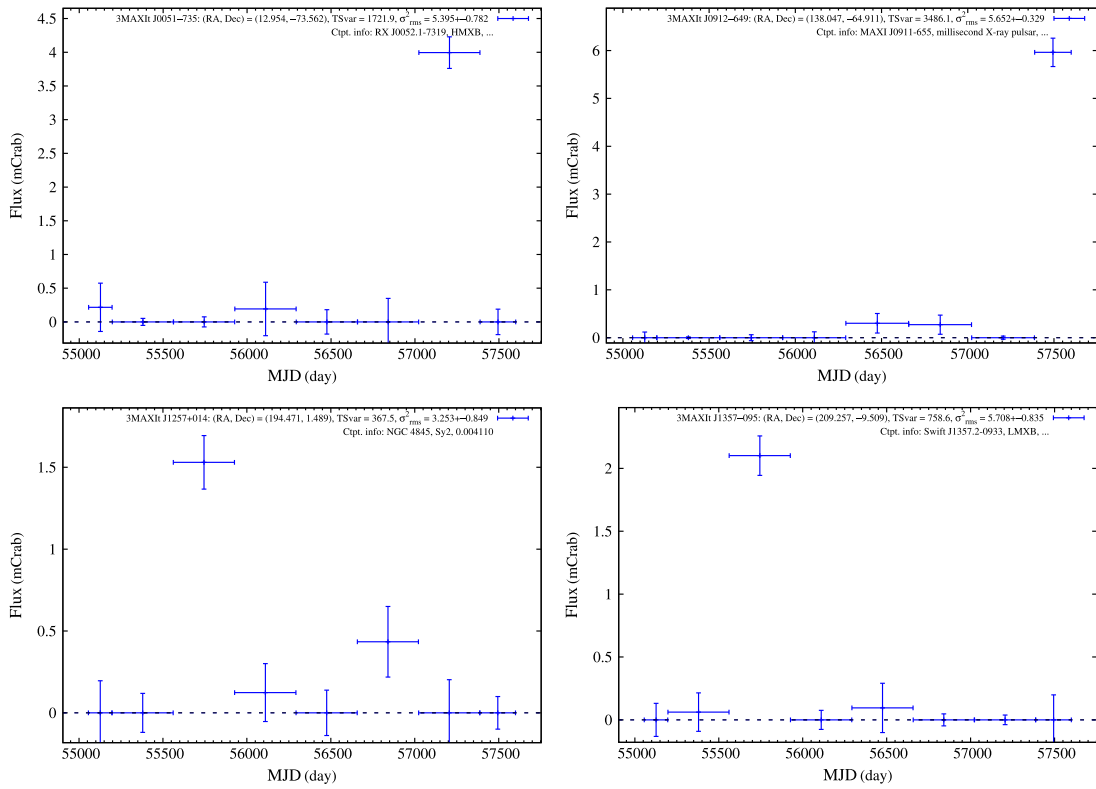


**Figure 7.** Light curves of the transient sources in the 4–10 keV band. The counterpart information (name, type, and redshift if available) is denoted in each figure. The data file of the light curves is available from the online supplementary tar.gz file.

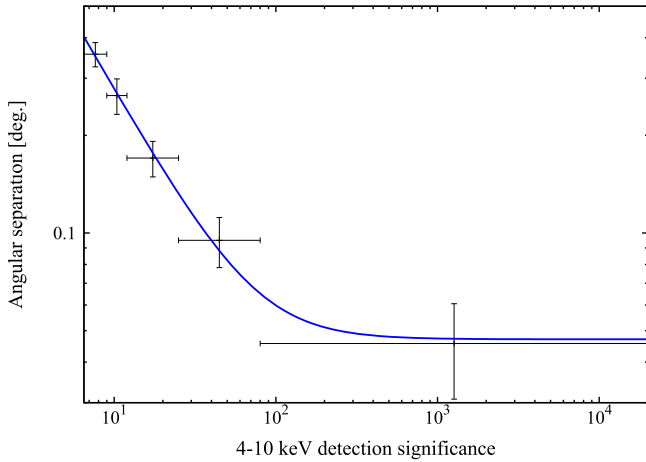


**Figure 8.** Correlation between the detection significance ( $s_{D,4-10\text{keV}}$ ) and the 90% confidence limit of the separation angles between the MAXI sources and their possible counterparts. The data (black crosses) can be described as  $\sqrt{(A/s_{D,4-10\text{keV}})^B + C^2}$  (blue solid line), where  $A = 2.27 \pm 0.05$ ,  $B = 1.74 \pm 0.02$ , and  $C = 0.047 \pm 0.001$ .

where  $F_i$ ,  $\Delta F_i$ ,  $F_{\text{const}}$ , and  $f$  denote the best-fit flux, statistical uncertainty, 7-year averaged flux, and systematic error (i.e., 1.4%), respectively, at the  $i$ th time bin.  $\text{TS}_{\text{var}}$  follows the chi-squared distribution when the number of bins is large. If  $\text{TS}_{\text{var}} > 18.48$ , we can reject the null hypothesis that the flux is constant at the 99% confidence level for 7 degrees of freedom. Next, we derive the excess variance ( $\sigma_{\text{rms}}^2$ ) following

Vaughan et al. (2003), or Equations (3) and (4) in Hori et al. (2018), to investigate the strength of flux variations.  $\text{TS}_{\text{var}}$  and  $\sigma_{\text{rms}}$  are listed in Table 1.

### 3.2. Transient Event Search

We systematically search for transient events that are missed in the catalog based on the 7-year integrated images. First, we create the significance maps in the individual years in the same manner as described in Section 2.2.1, using the best-fit model only including the cataloged sources. We then identify residuals with nominal significances above  $5.5\sigma$  as the candidates of transients. Then, we perform the image fitting by including their PSFs in the model in addition to those of the catalog sources. Four transient sources are found to show significances of  $s_{D,4-10\text{keV}} \geq 6.5$  in a time bin. Table 3 and Figure 7 present their X-ray properties and the light curves, respectively. Their coordinates are estimated from a period where the source shows the highest significance among all the time bins. Note that circular regions with a  $3^\circ$  radius around the very bright sources Sco X-1, Cyg X-2, and the Crab Nebula are excluded from this analysis to avoid fake source detection due to systematic errors in the PSF calibration.

## 4. Counterparts of Detected X-Ray Sources

### 4.1. Positional Cross-matching with Other X-Ray Catalogs

Identification of the X-ray sources is an important task for the statistical use of the catalog. To find possible counterparts of our

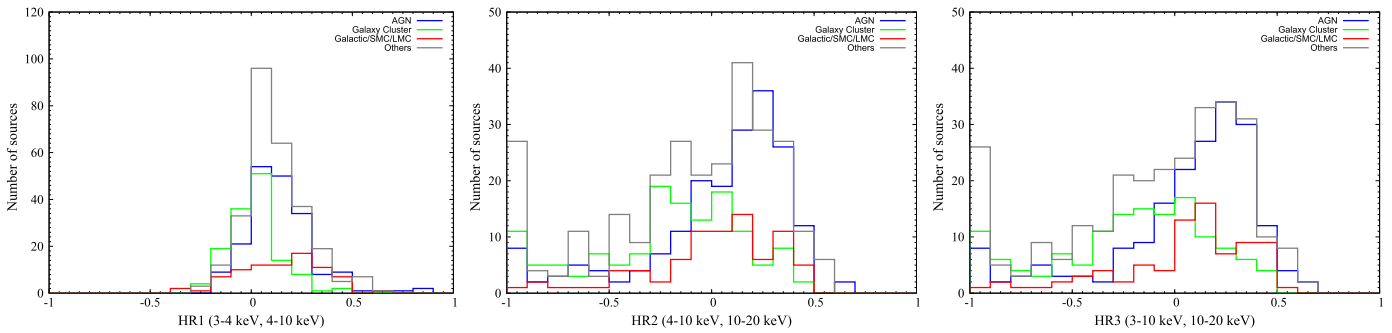


**Figure 9.** Histograms of the HRs. Here the MAXI sources are categorized into four types: AGN (blue), galaxy cluster (green), Galactic/SMC/LMC source (red), and others (gray).

**Table 4**  
Numbers of MAXI Sources Positionally Matched with Other Catalogs

Catalog Name	BAT105	4U	XTEASMLONG	MCXC	XMMSL2	1RXS	One Catalog Only <sup>a</sup>
BAT105	239(243) <sup>b</sup>	10	77	10	97	133	75
4U	...	17(17) <sup>b</sup>	12	4	8	11	2
XTEASMLONG	...	...	94(95) <sup>b</sup>	1	43	61	5
MCXC	...	...	...	152(164) <sup>b</sup>	16	66	82
XMMSL2	...	...	...	...	198(226) <sup>b</sup>	98	77
1RXS	...	...	...	...	...	250(251) <sup>b</sup>	48

**Notes.** The numbers of MAXI sources matched with both catalogs given in the first column and first row are listed.

<sup>a</sup> Numbers of the MAXI sources matched only with one catalog given in the first column.

<sup>b</sup> Numbers in parentheses represent those of total matched sources in each catalog.

catalog sources including the transients (hereafter we call them “the third MAXI sources”), we spatially cross-match them to those in other X-ray catalogs in the following order: the *Swift*/BAT 105-month catalog (BAT105; Oh et al. 2018), the *Uhuru* fourth catalog (4U; Forman et al. 1978), the *RXTE* All-Sky Monitor long-term observed source table (XTEASMLONG<sup>16</sup>), Meta-Catalog of X-Ray Detected Clusters of Galaxies (MCXC; Piffaretti et al. 2011), the *XMM-Newton* slew survey catalog (XMMSL2<sup>17</sup>), and the *ROSAT* all-sky survey bright source catalog (1RXS; Voges et al. 1999). To reduce false identifications, we only take account of XMMSL2 and 1RXS sources brighter than  $>1.0 \times 10^{-12} \text{ erg cm}^{-2} \text{ s}^{-1}$  and  $>0.30 \text{ counts s}^{-1}$ , respectively. This is a flux corresponding to 0.3 mCrab when the Crab spectrum is assumed. The statistical positional errors of the third MAXI sources ( $\sigma_{\text{stat}}$ ) are evaluated as  $\sqrt{dx^2 + dy^2}$ , where  $dx$  and  $dy$  are one-dimensional spatial errors in perpendicular directions at the  $1\sigma$  level. A systematic error ( $\sigma_{\text{sys}}$ ) is further added to the statistical ones as  $\sigma_{\text{pos}} = \sqrt{\sigma_{\text{stat}}^2 + \sigma_{\text{sys}}^2}$ . We adopt  $\sigma_{\text{sys}} = 0.03$ , determined to self-consistently match the cross-matching result (see Section 4.3 and Figure 8). Here, we identify a counterpart if its position falls within  $2.5\sigma_{\text{pos}}$  of a third MAXI source. Using several representative sources, we have verified that the radius of  $2.5\sigma_{\text{stat}}$  typically corresponds to that of the 95% confidence contour for the source positions where the  $C$  value in Equation (1) is increased from the best value by 6.0. The positional errors in the reference catalogs are ignored. Note that if we find more than one source as counterpart candidates, we list the object nearest to the MAXI position. The cross-matching result is summarized in Table 2, and the numbers of the positionally matched MAXI sources are listed in Table 4. The breakdown of

**Table 5**  
Numbers of Sources in Each Category

Category	Number of Sources
Unknown <sup>a</sup>	14
Galaxy clusters	135
Galaxies	2
Seyfert galaxies	142
Blazars	48
Cataclysmic variables/stars	54
Pulsars	2
X-ray binaries	24
Confused	1
Unmatched <sup>b</sup>	260
Total	682

**Notes.**

<sup>a</sup> Sources that have possible counterparts in at least one of the cross-matched catalogs but have no classification.

<sup>b</sup> Sources that have no counterparts in the cross-matched catalogs.

the source types is seen in Table 5. The counterparts of the transients (Section 3.2) are also identified from the *Swift*/BAT Hard X-ray Transient Monitor catalog<sup>18</sup> in the same manner, but with the  $3.0\sigma$  positional errors, because the probability of false matching is much lower than in the other cases (see Section 4.2).

In some cases, we suspect that a matched counterpart is likely incorrect, judging from the X-ray properties (i.e., the time variability, HRs, and observed fluxes). Also, some bright galaxy clusters are not identified from the automatic cross-matching. This could be because our PSF model is developed so that it reproduces a point source and would not properly fit

<sup>16</sup> <https://heasarc.gsfc.nasa.gov/W3Browse/xte/xteasmlong.html>

<sup>17</sup> <https://www.cosmos.esa.int/web/xmm-newton/xmmsl2-ug>

<sup>18</sup> <https://swift.gsfc.nasa.gov/results/transients/>

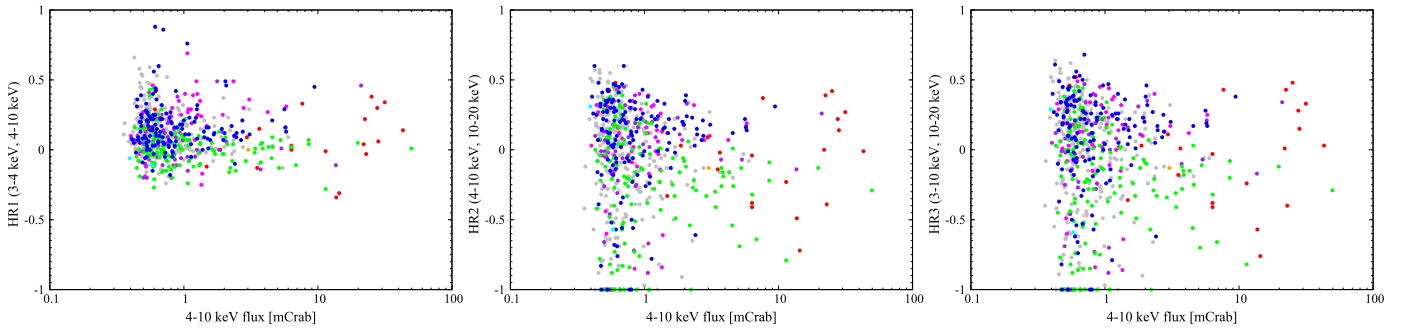


**Figure 10.** Scatter plots between the HRs and the 4–10 keV flux. The color definition is the same as in Figure 3.

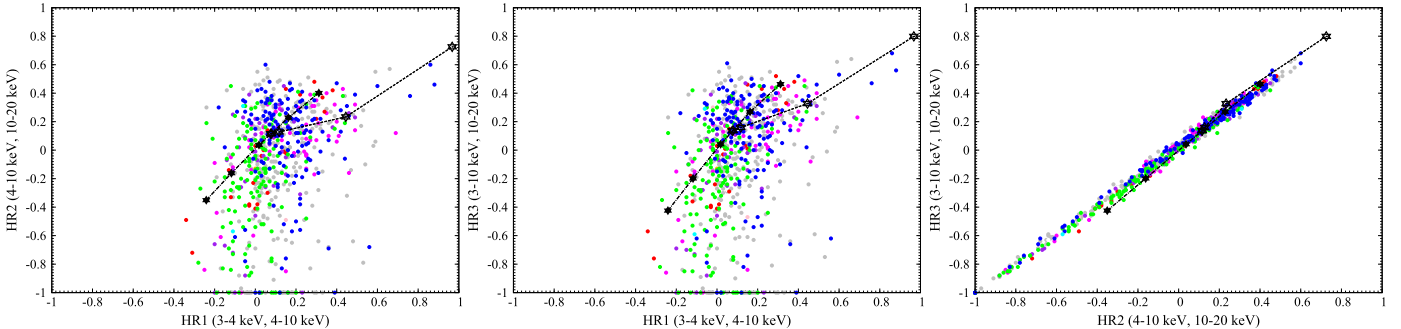


**Figure 11.** X-ray color–color plots among the three HRs. The filled stars and dot-dashed lines illustrate the HR track for a power-law model without intrinsic absorption. The stars from upper right to lower left correspond to photon indices from 1.0 to 3.0 with a step of 0.5. The open stars and dashed lines present the track for an absorbed power-law model with a photon index of 1.8. The open stars from lower left to upper right correspond to  $\log N_{\text{H}}/\text{cm}^{-2}$  from 20.0 to 24.0 with a step of 1.0. The color definition is the same as those in Figure 3.

such extended sources. More plausible counterparts for them are listed in the catalog, with the associated comments in Column (9).

#### 4.2. Probability of Chance Coincidence

The above cross-matching is based only on the separation angles between the MAXI and other reference sources, and some counterparts are incorrectly identified because they just coincidentally fall within the positional error of a third MAXI source. We derive the expected number of such events by combining integrated positional errors of the MAXI sources used for each cross-matching and source number densities (i.e., source number divided by our survey area) of the reference catalogs. We find that 10, 1, 2, 11, 11, and 7 MAXI sources may be misidentified in referring to BAT105, 4U, XTEASMLONG, MCXC, XMMSL2, and 1RXS, respectively. Note that due to the incomplete all-sky survey of XMMSL2, its derived value should be regarded as a lower limit. If we use only MCXC and *Swift*/BAT 105-month catalogs, similarly to the case of Hiroi et al. (2013), who used MCXC and the *Swift*/BAT 70-month catalog (Baumgartner et al. 2013), the expected fraction of the false identification is  $\sim 0.03$ . This remains at the same level as in the 37-month catalog, in spite of the increased source number in the 7-year MAXI and *Swift*/BAT 105-month catalogs. This small value is likely because the systematic errors of the PSF model are reduced in our catalog.

#### 4.3. Systematic Positional Error

Using the results in Section 4.1, we examine the separation angles between the MAXI sources and their possible counterparts as a function of the detection significance ( $s_{\text{D},4-10 \text{ keV}}$ ). Figure 8 plots the 90% confidence limit of the separation angles, estimated in each significance bin. For consistency,

we fit the data with the same equation as that in Hiroi et al. (2013),  $\sqrt{(A/s_{\text{D},4-10 \text{ keV}})^B + C^2}$ . The best-fit parameters are  $A = 2.27 \pm 0.05$ ,  $B = 1.74 \pm 0.02$ , and  $C = 0.047 \pm 0.001$ , suggesting the systematic error at a 90% confidence limit of  $\approx 0^\circ.047$ . The corresponding  $1\sigma$  error is  $\sim 0^\circ.03$ . The systematic error is successfully reduced from the previous works ( $\approx 0^\circ.05$ ; Hiroi et al. 2011, 2013).

## 5. Statistical Properties of Our Catalog

### 5.1. Correlations among X-Ray Properties

In this section, we describe basic properties of our catalog based on the parameters constrained so far: the fluxes, the HRs, and the time variability index ( $\text{TS}_{\text{var}}$ ). Here, we simply categorize the third MAXI sources into four types: AGN (i.e., Seyfert galaxies and blazars), galaxy cluster, Galactic/Small/Large Magellanic Cloud (SMC/LMC) source (i.e., cataclysmic variables/stars, X-ray binaries, and pulsars), and the others. The HR distributions are shown in Figure 9, and the scatter plots between the HRs and the 4–10 keV fluxes are shown in Figure 10. A noticeable point is that the HRs of AGNs are typically harder than those of the galaxy clusters. The difference is more clearly seen in the HRs using the 10–20 keV band. This is likely to be a natural consequence of the difference in their typical spectra; galaxy clusters are bright in soft X-ray bands by optically thin thermal emission, whereas AGNs exhibit harder spectral profiles, roughly described with a power-law component with a photon index of  $\sim 1.4$ – $2.4$  (e.g., Ueda et al. 2014; Kawamuro et al. 2016b). Strong absorption, often seen in AGNs, hardens their spectrum even more, and thereby higher HRs are expected. A more detailed view can be obtained from X-ray color–color plots in Figure 11, which

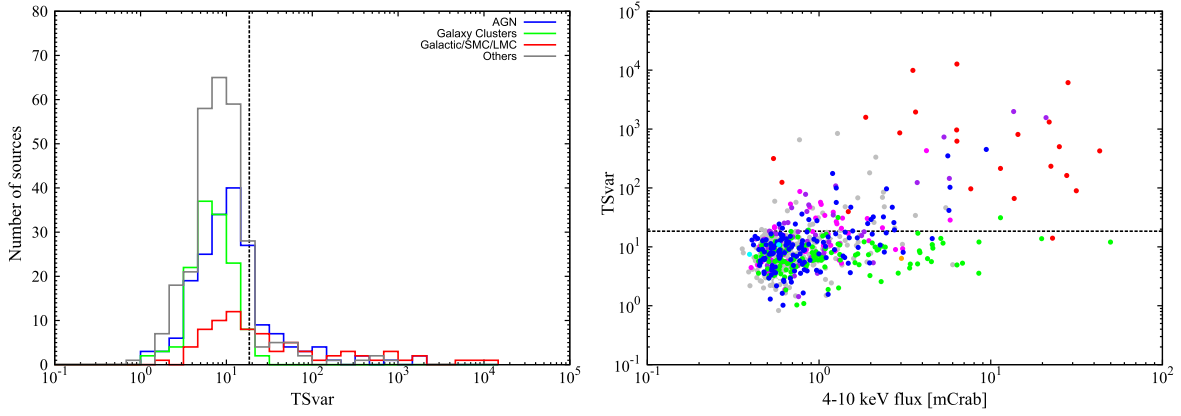


**Figure 12.** Left: histogram of the time variability index ( $TS_{\text{var}}$ ). The color definition is the same as that in Figure 9. Right: scatter plot between the 4–10 keV flux and  $TS_{\text{var}}$ . The colors are the same as in Figure 3. In both figures, variable sources are located in the area of  $TS_{\text{var}} > 18.48$  (dashed line), corresponding to a 99% confidence limit.

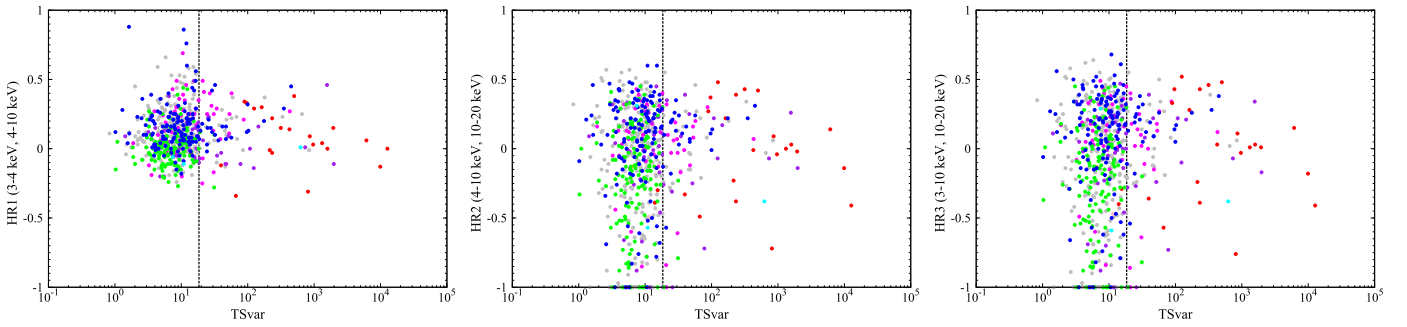


**Figure 13.** Scatter plots between the HRs and  $TS_{\text{var}}$ . The colors are the same as in Figure 3.

overplots HR tracks predicted from a single (absorbed) power-law model based on Figure 4.

Figure 12 shows the histogram of the time variability index ( $TS_{\text{var}}$ ) and its scatter plot against the 4–10 keV flux. Also, Figure 13 plots the HRs with respect to  $TS_{\text{var}}$ . Most of the galaxy clusters have no significant flux variation, with  $TS_{\text{var}} < 18.48$ , but there are two exceptions showing moderate  $TS_{\text{var}}$  values of  $\approx 30$ . One is 3MAXI J1231+122, identified as the Virgo Cluster, and this apparent variability may be due to uncertainties associated with our PSF model, which assumes a point source, and/or the presence of an AGN in M87 (Wong et al. 2017). The other source, 3MAXI J1702+339, is located near the bright, variable source Her X-1, and part of its flux could be contaminated by Her X-1, causing the fake variability.

### 5.2. Comparison with the Swift/BAT 105-month Catalog

Here we briefly view the nature of the third MAXI sources that have a single counterpart in the BAT105. Figure 14 plots the correlation between the 4–10 keV and 14–195 keV fluxes, together with the flux ratios predicted from unabsorbed power-law models with three different photon indices ( $\Gamma = 1.7, 2.0,$  and  $2.5$ ). Note that we use the 4–10 keV fluxes estimated through the conversion factor of  $1.21 \times 10^{-11} \text{ erg cm}^{-2} \text{ s}^{-1} \text{ mCrab}^{-1}$ , while the 14–195 keV fluxes are retrieved from Oh et al. (2018). As seen in Figure 14, most of the MAXI sources have soft spectra, corresponding to photon indices larger than 1.7.

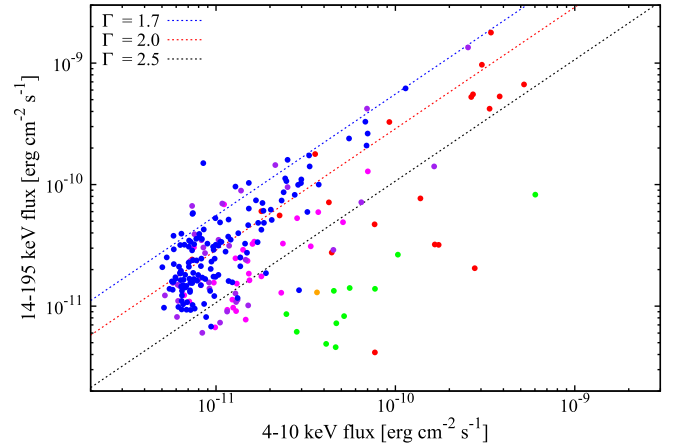


**Figure 14.** Scatter plot between the 4–10 keV and 14–195 keV fluxes for MAXI sources having a single counterpart in the *Swift*/BAT 105-month catalog. The 4–10 keV fluxes are calculated with a conversion factor of  $1.21 \times 10^{-11} \text{ erg cm}^{-2} \text{ s}^{-1} \text{ mCrab}^{-1}$ , while the 14–195 keV ones are retrieved from the *Swift*/BAT 105-month catalog (Oh et al. 2018). Dashed lines present the relations for an unabsorbed power-law spectrum with different photon indices:  $\Gamma = 2.5$  (black),  $\Gamma = 2.0$  (red), and  $\Gamma = 1.7$  (blue).

### 5.3. log N–log S Relation

We present the log  $N$ –log  $S$  relation, the cumulative flux distributions of the sources detected at  $s_{D,4-10 \text{ keV}} \geq 6.5$ . To derive it, we estimate the sensitivity at every sky position by combining the background counts and the effective exposure map, given in Figure 1 of Hori et al. (2018). The effective

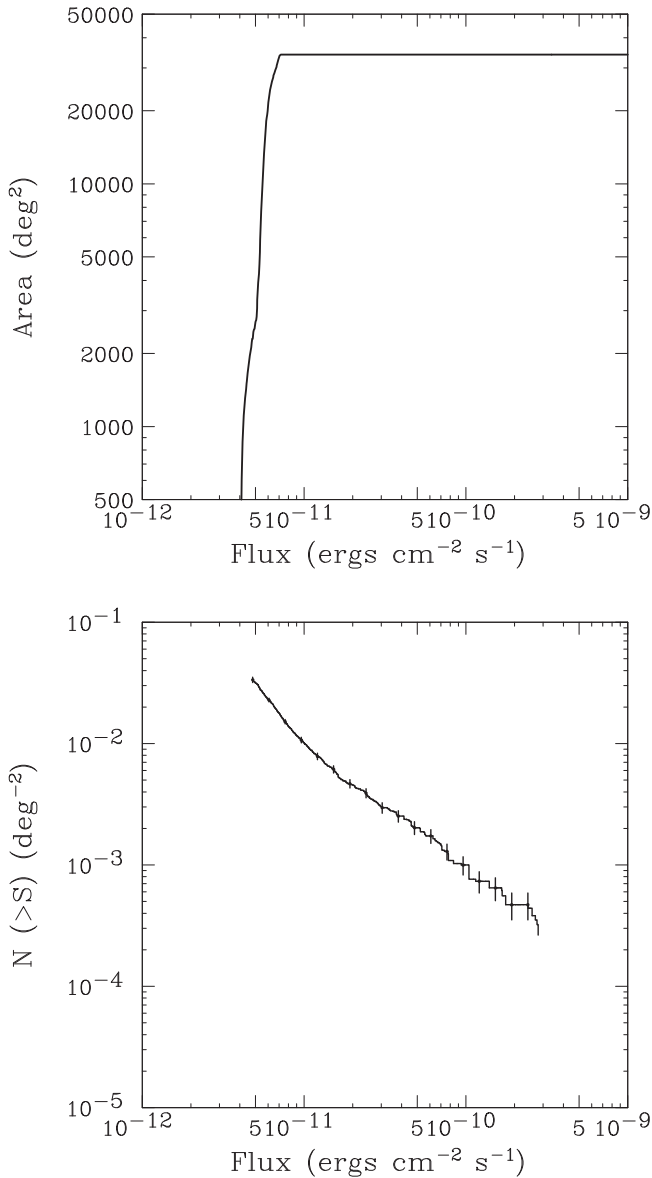


**Figure 15.** Top panel: survey area plotted against 4–10 keV flux for the MAXI/GSC 7-year survey at  $|b| > 10^\circ$ . Bottom panel:  $\log N$ – $\log S$  relation in the integral form.

exposure map, in units of  $\text{cm}^2 \text{s}$ , is estimated via simulation of the cosmic X-ray background, with uniform brightness (see Hori et al. 2018, for more details). The survey area as a function of the sensitivity (i.e., the area curve) is displayed in the top panel of Figure 15. From this curve, we can find that our survey is complete, in half of the high Galactic latitude sky ( $|b| > 10^\circ$ ), down to  $5.9 \times 10^{-12} \text{ erg cm}^{-2} \text{ s}^{-1}$ , superior to the 37-month catalog (i.e.,  $7.5 \times 10^{-12} \text{ erg cm}^{-2} \text{ s}^{-1}$ ; Hiroi et al. 2013). The deepest sensitivity of  $\sim 4 \times 10^{-12} \text{ erg cm}^{-2} \text{ s}^{-1}$  is consistent with the lowest flux among the actually detected sources.

We divide the number of sources with fluxes of  $S \sim S + dS$  by the survey area at  $S$  and obtain the  $\log N$ – $\log S$  relation in the differential form. By integrating it, we obtain the number density  $N(>S)$  of total sources having fluxes above  $S$  (bottom panel of Figure 15). At fluxes lower than  $8 \times 10^{-11} \text{ ergs cm}^{-2} \text{ s}^{-1}$ , the  $\log N$ – $\log S$  relation has a slightly steeper slope

than that expected for sources uniformly distributed in a static Euclidean universe (i.e.,  $N(>S) \propto S^{-1.5}$ ). This may be partially caused by the Eddington bias (i.e., fainter sources than the sensitivity limit emerge owing to statistical fluctuation).

## 6. Summary

We have provided the third MAXI/GSC X-ray source catalog in the high-latitude sky ( $b > 10^\circ$ ) utilizing the first 7-year (2009 August 13 to 2016 July 31) data in the 4–10 keV band. The catalog contains 682 X-ray sources detected at  $s_{\text{D},4-10 \text{ keV}} \geq 6.5$ . Over half of the survey area, the 4–10 keV band sensitivity reaches  $\sim 5.9 \times 10^{-12} \text{ erg cm}^{-2} \text{ s}^{-1}$ , which is the highest ever achieved as an all-sky X-ray survey in a similar energy band. The source number has increased by a factor of  $\approx 1.4$  compared with the 37-month MAXI/GSC catalog (Hiroi et al. 2013), which adopted  $s_{\text{D},4-10 \text{ keV}} \geq 7$  as the detection threshold. We have cross-matched the cataloged sources with those in the other X-ray catalogs (BAT105, 4U, XTEASM-LONG, MCXC, XMMSL2, and 1RXS) and found the counterparts of 422 sources.

In addition to the basic properties in the 4–10 keV band, we provide the 7-year averaged fluxes in the 3–4 keV, 10–20 keV, and 3–10 keV bands, as well as their HRs. The HRs, particularly the ones using the 10–20 keV fluxes, seem to be the most helpful to discriminate between AGNs and galaxy clusters. We have also built the database of the 1-year-bin 4–10 keV light curves, with their variability index ( $\text{TS}_{\text{var}}$ ) and the excess variance ( $\sigma_{\text{rms}}^2$ ). We find that the compact objects, such as X-ray binaries and AGNs, show strong variability ( $\text{TS}_{\text{var}} > 18.48$ ), demonstrating that the variability is a key to uncovering the nature of unidentified X-ray sources. Future follow-up observations with a higher spatial and timing resolution are encouraged to associate the unidentified sources in our catalog with those in other catalogs, for improving the completeness of the catalog so that it can be used in statistical studies.

We have searched the 1-year time-sliced data for transient sources (Section 3.2) and found four objects that are not detected from the 7-year accumulated data (Table 3). They are indeed classified as transient compact objects (i.e., X-ray binary, pulsar, and AGN/tidal disruption event).

We thank Kyuseok Oh for providing the Swift/BAT 105-month catalog prior to the official publication. Part of this work was financially supported by the Grant-in-Aid for JSPS Fellows for young researchers (T.K. and T.H.), for Scientific Research 17H06362 (Y.U., N.K., T.M., H.N., and A.Y.) and 17K05384 (Y.U.), and for Young Scientists (B) 16K17672 (M.S.). M.S. acknowledges support by the Special Postdoctoral Researchers Program at RIKEN. This research has made use of MAXI data provided by RIKEN, JAXA, and the MAXI team.

## ORCID iDs

T. Kawamuro <https://orcid.org/0000-0002-6808-2052>  
 Y. Ueda <https://orcid.org/0000-0001-7821-6715>  
 T. Hori <https://orcid.org/0000-0001-8204-790X>  
 N. Kawai <https://orcid.org/0000-0001-9656-0261>  
 A. Tanimoto <https://orcid.org/0000-0002-0114-5581>  
 Y. Tsuboi <https://orcid.org/0000-0001-9943-0024>  
 Y. Sugawara <https://orcid.org/0000-0001-6749-1199>

## References

- Abeyssekara, A. U., Archambault, S., Archer, A., et al. 2017, *ApJ*, **836**, 205
- Arnaud, K. A. 1996, *adass V*, **101**, 17
- Baumgartner, W. H., Tueller, J., Markwardt, C. B., et al. 2013, *ApJS*, **207**, 19
- Cash, W. 1979, *ApJ*, **228**, 939
- Dalabuit, E., & Meyer, S. 1972, *A&A*, **20**, 415
- Eguchi, S., Hiroi, K., Ueda, Y., et al. 2009, in *Proceedings of the RIKEN Symposium, Astrophysics with All-Sky X-Ray Observations*, ed. T. Mihara & M. Serino, **44**
- Forman, W., Jones, C., Cominsky, L., et al. 1978, *ApJS*, **38**, 357
- Gehrels, N., Chincarini, G., Giommi, P., et al. 2004, *ApJ*, **611**, 1005
- Górski, K. M., Hivon, E., Banday, A. J., et al. 2005, *ApJ*, **622**, 759
- Hiroi, K., Ueda, Y., Hayashida, M., et al. 2013, *ApJS*, **207**, 36
- Hiroi, K., Ueda, Y., Isobe, N., et al. 2011, *PASJ*, **63**, 677
- Hori, T., Shidatsu, M., Ueda, Y., et al. 2018, *ApJS*, **235**, 7
- Inoue, Y., & Tanaka, Y. T. 2016, *ApJ*, **828**, 13
- Isobe, N., Kawamuro, T., Oyabu, S., et al. 2016, *PASJ*, **68**, 98
- Isobe, N., Sato, R., Ueda, Y., et al. 2015, *ApJ*, **798**, 27
- Kawamuro, T., Ueda, Y., Shidatsu, M., et al. 2016a, *PASJ*, **68**, 58
- Kawamuro, T., Ueda, Y., Tazaki, F., Ricci, C., & Terashima, Y. 2016b, *ApJS*, **225**, 14
- Matsuoka, M., Kawasaki, K., Ueno, S., et al. 2009, *PASJ*, **61**, 999
- Mihara, T., Nakajima, M., Sugizaki, M., et al. 2011, *PASJ*, **63**, 623
- Morii, M., Tomida, H., Kimura, M., et al. 2013, *ApJ*, **779**, 118
- Negoro, H., Kohama, M., Serino, M., et al. 2016, *PASJ*, **68**, S1
- Negoro, H., Ozawa, H., Suwa, F., et al. 2012, *adass XXI*, **461**, 797
- Nolan, P. L., Abdo, A. A., Ackermann, M., et al. 2012, *ApJS*, **199**, 31
- Oh, K., Koss, M., Markwardt, C. B., et al. 2018, *ApJS*, **235**, 4
- Piffaretti, R., Arnaud, M., Pratt, G. W., Pointecouteau, E., & Melin, J.-B. 2011, *A&A*, **534**, A109
- Serino, M., Shidatsu, M., Ueda, Y., et al. 2015, *PASJ*, **67**, 30
- Shidatsu, M., Tachibana, Y., Yoshii, T., et al. 2017a, *ApJ*, **850**, 155
- Shidatsu, M., Ueda, Y., Kawamuro, T., et al. 2017b, 7 Years of MAXI: Monitoring X-ray Transients, 29, Online at <https://indico2.riken.jp/indico/conferenceDisplay.py?confId=2357>
- Sugizaki, M., Mihara, T., Serino, M., et al. 2011, *PASJ*, **63**, 635
- Tachibana, Y., Kawamuro, T., Ueda, Y., et al. 2016, *PASJ*, **68**, S25
- Terashima, Y., Hirata, Y., Awaki, H., et al. 2015, *ApJ*, **814**, 11
- Tomida, H., Tsunemi, H., Kimura, M., et al. 2011, *PASJ*, **63**, 397
- Tomsick, J. A., Lansbury, G. B., Rahoui, F., et al. 2017, *ApJS*, **230**, 25
- Truemper, J. 1982, *AdSpR*, **2**, 241
- Ueda, Y., Akiyama, M., Hasinger, G., Miyaji, T., & Watson, M. G. 2014, *ApJ*, **786**, 104
- Ueda, Y., Hiroi, K., Isobe, N., et al. 2011, *PASJ*, **63**, S937
- Vaughan, S., Edelson, R., Warwick, R. S., & Uttley, P. 2003, *MNRAS*, **345**, 1271
- Voges, W., Aschenbach, B., Boller, T., et al. 1999, *A&A*, **349**, 389
- Wilson-Hodge, C. A., Cherry, M. L., Case, G. L., et al. 2011, *ApJL*, **727**, L40
- Winkler, C., Courvoisier, T. J.-L., Di Cocco, G., et al. 2003, *A&A*, **411**, L1
- Wong, K.-W., Nemmen, R. S., Irwin, J. A., & Lin, D. 2017, *ApJL*, **849**, L17